Electronic Supplementary Material (ESI) for Physical Chemistry Chemical Physics.

Supporting Information for

Polarization-tunable interfacial properties in monolayer-MoS_2 transistors integrated with ferroelectric $BiAlO_3$(0001) polar surfaces

Jin Yuan, Jian-Qing Dai,* Yu-Zhu Liu, and Miao-Wei Zhao

Faculty of Materials Science and Engineering, Kunming University of Science and Technology, Kunming 650093, P. R. China

*Corresponding author. Fax: +86 871 65107922.

E-mail address: djqkust@sina.com (J.-Q. Dai).

ORCID: 0000-0003-4352-0789 (Jian-Qing Dai).

Table S1 Calculated lattice constants of BAO, BN, MoS_2, and Gr, as well as the strain state of each component in eight FHSs. Here, the positive sign denotes tensile strain and the experimental lattice constants are also showed for demonstrating credibility of the results.

Material	Lattice constant	Lattice constant[a]	Strain
BAO	a = b = 5.363 Å	a = b = 5.375 Å	+1.4%
BN	a = b = 2.505 Å	a = b = 2.500 Å	+8.6%
MoS_2	a = b = 3.140 Å	a = b = 3.151 Å	0
Gr	a = b = 2.470 Å	a = b = 2.460 Å	+10.1%

[a] Experimental lattice constants of BAO,[1] BN,[2] MoS_2,[3] and Gr.[4]

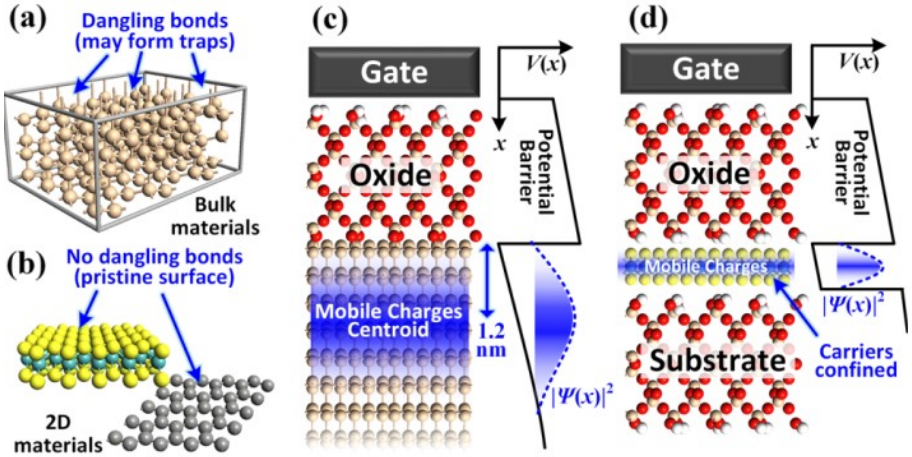

Fig. S1 Schematic illustrating advantages of 2D materials: surfaces of (a) bulk and (b) 2D materials. The pristine interfaces (without out-of-plane dangling bonds) of 2D materials help reduce the interface traps. Mobile charge distribution in (c) bulk and (d) 2D crystals used as channel materials. $V(x)$ and $|\psi(x)|^2$ represent the potential and the probability density of the electronic charges, respectively. The carrier confinement effect in 2D materials leads to better gate control than bulk materials.[5]

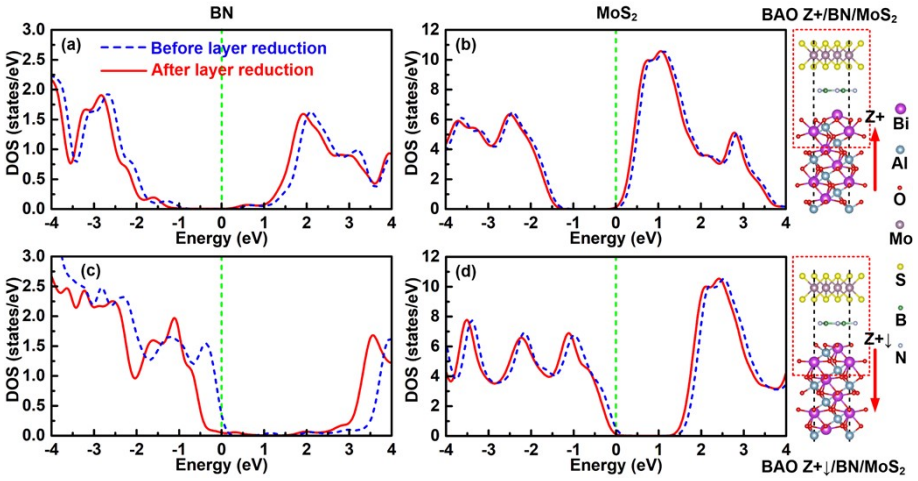

Fig. S2 PDOS of (a and c) BN interlayer and (b and d) MoS_2 overlayer in the (a and b) BAO Z+/BN/MoS_2 and (c and d) BAO Z+↓/BN/MoS_2 FHSs with five 1 × 1 Bi-Al-O_3 trilayers plus surface termination. Here, the PDOS of BN interlayer and MoS_2 overlayer after removing backside four trilayers of the

BAO(0001) slabs are also shown for comparison, the right insets show corresponding optimized FHSs (the FHSs after removing the backside four trilayers are marked by red short dash rectangles and the red arrows show the polarization directions), and the E_F is set to the energy of 0 eV.

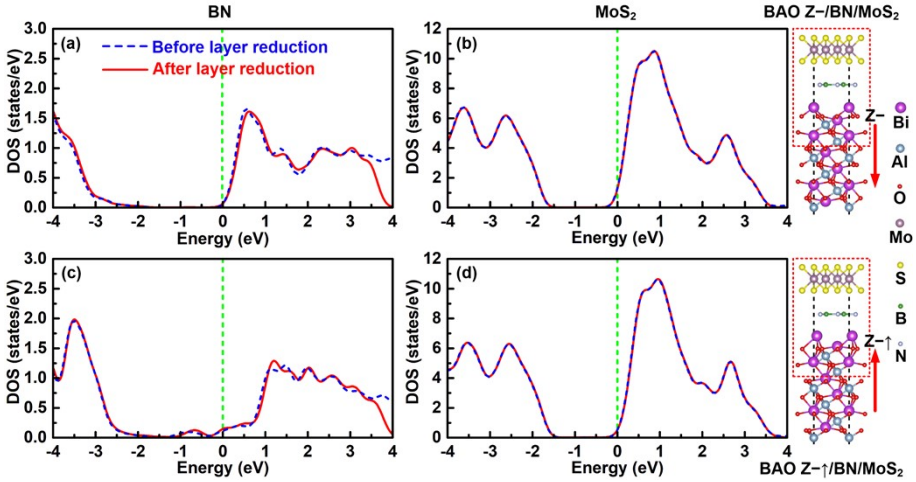

Fig. S3 PDOS of (a and c) BN interlayer and (b and d) MoS_2 overlayer in the (a and b) BAO Z−/BN/MoS_2 and (c and d) BAO Z−↑/BN/MoS_2 FHSs with five 1 × 1 Bi-Al-O_3 trilayers plus surface termination. Here, the PDOS of BN interlayer and MoS_2 overlayer after removing backside four trilayers of the BAO(0001) slabs are also shown for comparison, the right insets show corresponding optimized FHSs (the FHSs after removing the backside four trilayers are marked by red short dash rectangles and the red arrows show the polarization directions), and the E_F is set to the energy of 0 eV.

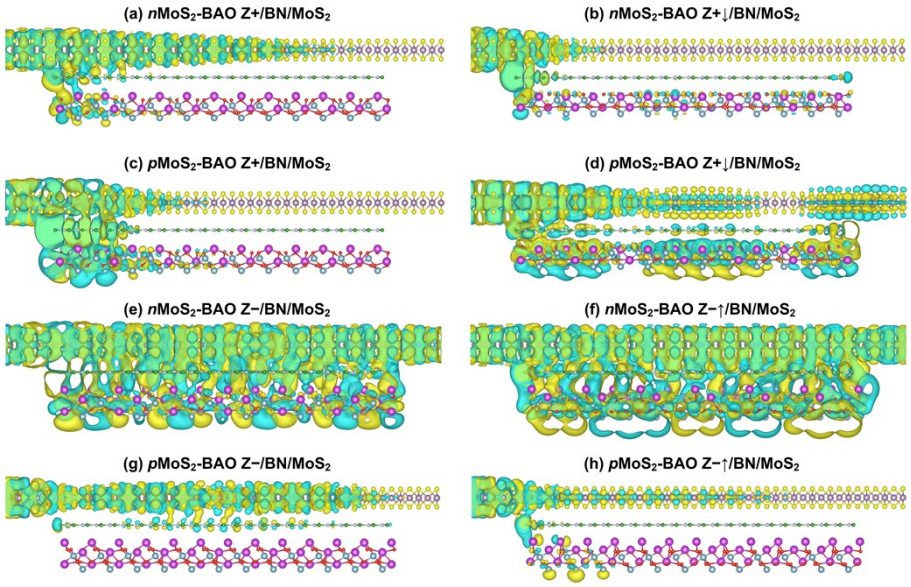

Fig. S4 Real-space scatting states of (a and b) *n*MoS_2-BAO Z+(Z+↓)/BN/MoS_2, (c and d) *p*MoS_2-BAO Z+(Z+↓)/BN/MoS_2, (e and f) *n*MoS_2-BAO Z−(Z−↑)/BN/MoS_2, and (g and h) *p*MoS_2-BAO Z−(Z−↑)/BN/MoS_2 FeFETs at the E_F.

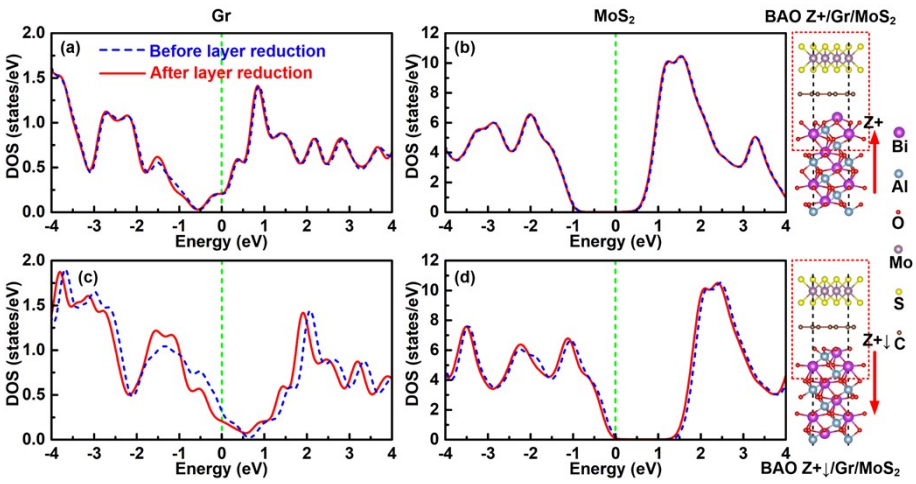

Fig. S5 PDOS of (a and c) Gr interlayer and (b and d) MoS_2 overlayer in the (a and b) BAO Z+/Gr/MoS_2 and (c and d) BAO Z+↓/Gr/MoS_2 FHSs with five 1 × 1 Bi-Al-O_3 trilayers plus surface termination. Here, the PDOS of Gr interlayer and MoS_2 overlayer after removing backside four trilayers of the BAO(0001) slabs are also shown for comparison, the right insets show corresponding optimized FHSs (the FHSs after removing the backside four trilayers are marked by red short dash rectangles and the red arrows show the polarization directions), and the E_F is set to the energy of 0 eV.

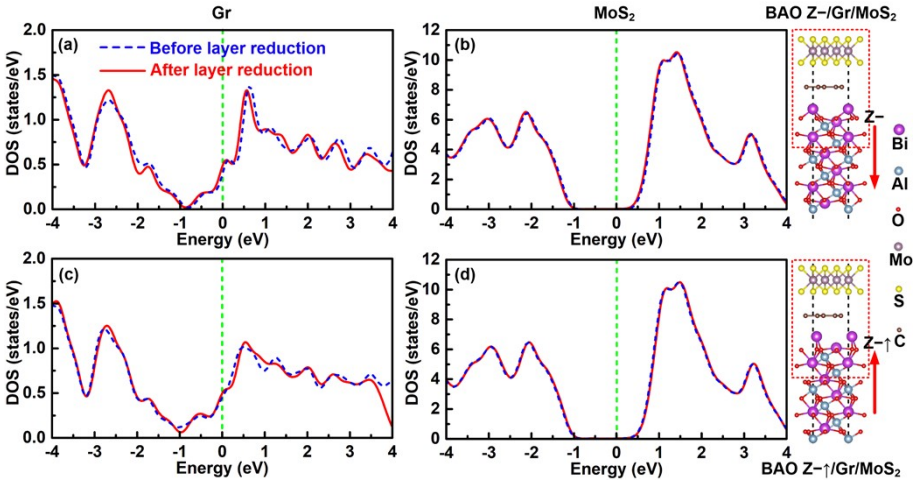

Fig. S6 PDOS of (a and c) Gr interlayer and (b and d) MoS_2 overlayer in the (a and b) BAO Z−/Gr/MoS_2 and (c and d) BAO Z−↑/Gr/MoS_2 FHSs with five 1 × 1 Bi-Al-O_3 trilayers plus surface termination. Here, the PDOS of Gr interlayer and MoS_2 overlayer after removing backside four trilayers of the BAO(0001) slabs are also shown for comparison, the right insets show corresponding optimized FHSs (the FHSs after removing the backside four trilayers are marked by red short dash rectangles and the red arrows show the polarization directions), and the E_F is set to the energy of 0 eV.

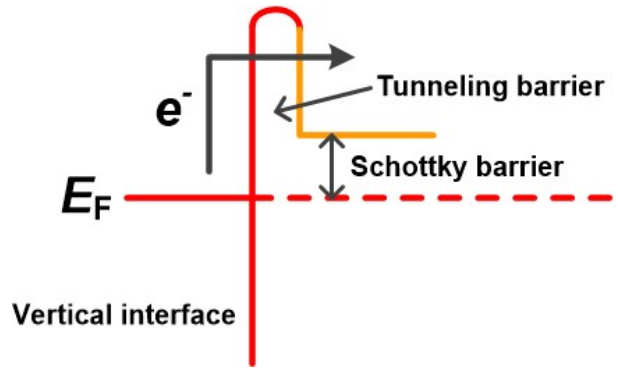

Fig. S7 Schematic diagram of electron tunneling across the vertical interface. Here, the tunneling and Schottky barriers are two key factors to evaluate the electron injection efficiency from the source region to channel.[6]

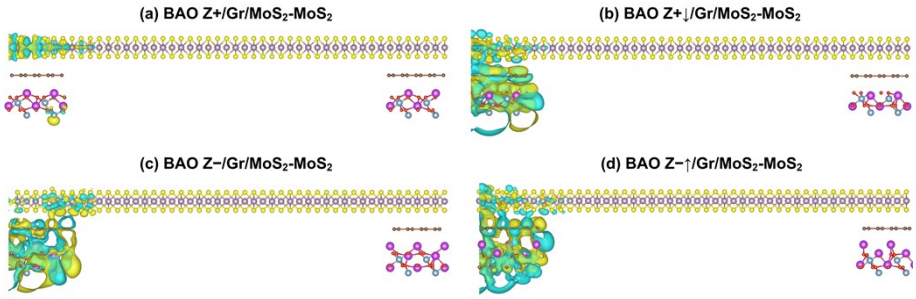

Fig. S8 Real-space scatting states of (a and b) BAO Z+(Z+↓)/Gr/MoS_2-MoS_2 and (c and d) BAO Z−(Z−↑)/Gr/MoS_2-MoS_2 FeFETs at the E_F.

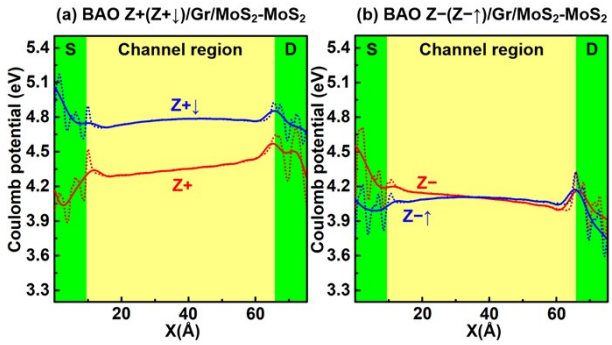

Fig. S9 Planar and macroscopic averaged Coulomb potential of (a) BAO Z+(Z+↓)/Gr/MoS_2-MoS_2 and (b) BAO Z−(Z−↑)/Gr/MoS_2-MoS_2 FeFETs. Here, the S (D) represents the source (drain) region and the red (blue) lines represent the devices before (after) polarization reversal.

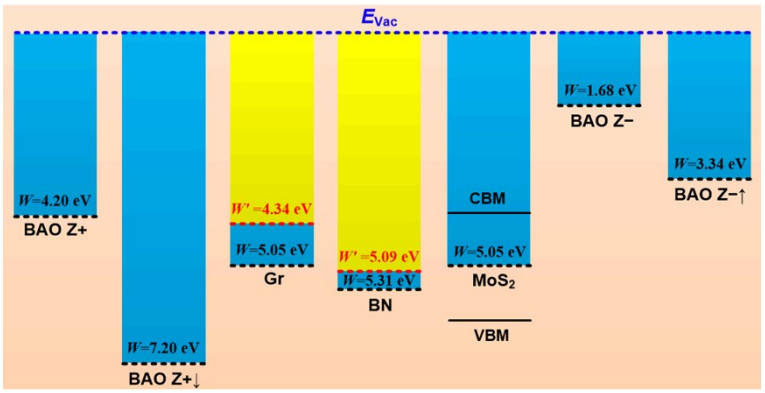

Fig. S10 Comparison of work function W of the BAO Z+(Z+↓) surface (with +1.4% tensile strain), BAO Z−(Z−↑) surface (with +1.4% tensile strain), BN layer (with +8.6% tensile strain), Gr layer (with +10.1% tensile strain), and MoS_2 layer (with 0 strain) before contact. Here, the black short dash lines represent E_F, the E_{Vac} represents the vacuum electrostatic potential energy of an electron, the VBM and CBM of intrinsic ML-MoS_2 are marked by black solid lines, and the work function W' (see the red short dash lines) of intrinsic Gr and BN layer with 0 strain is also showed to demonstrate credibility of the results.

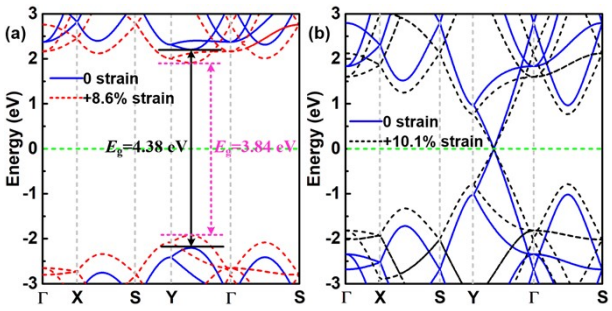

Fig. S11 Band structures of 2 × 2√3 (a) ML-BN with 0 strain (blue solid line) and +8.6% tensile strain (red short dash line) and (b) Gr with 0 strain (blue solid line) and +10.1% tensile strain (black short dash line). Here, the E_F is set to the energy of 0 eV and the high-symmetry points of Brillouin zone are shown in Fig. 2.

---

[1] A. A. Belik, T. Wuernisha, T. Kamiyama, and K. Mori, High-pressure synthesis, crystal structures, and properties of perovskite-like $BiAlO_3$ and pyroxene-like $BiGaO_3$, Chem. Mater. 18 (2006) 133-139.

[2] L. Liu, J. Park, D. A. Siegel, K. F. McCarty, K. W. Clark, W. Deng, L. Basile, J. C. Idrobo, A.-P. Li, and G. Gu, Heteroepitaxial growth of two-dimensional hexagonal boron nitride templated by graphene edges, Science 343 (2014) 163-167.

[3] H.-G. Kim and H. J. Choi, Thickness dependence of work function, ionization energy, and electron affinity of Mo and W dichalcogenides from DFT and GW calculations, Phys. Rev. B 103 (2021) 085404.

[4] D. Shin and A. A. Demkov, Theoretical investigation of the band alignment of graphene on a polar $SrTiO_3$(111) surface, Phys. Rev. B: Condens. Matter Mater. Phys. 97 (2018) 075423.

[5] J. Kang, W. Liu, D. Sarkar, D. Jena, and K. Banerjee, Computational study of metal contacts to monolayer transition-metal dichalcogenide semiconductors, Phys. Rev. X 4 (2014) 031005.

[6] Z-W Zhang, Z.-S. Liu, J.-J. Zhang, B.-N. Sun, D.-F. Zou, G.-Z. Nie, M. Chen, Y.-Q. Zhao, and S. Jiang, Interfacial contact barrier and charge carrier transport of MoS_2/metal(001) heterostructures, Phys. Chem.

Chem. Phys., 25 (2023) 9548-9558.